Quantitative tomographic imaging of intermolecular FRET in small animals

Vivek Venugopal,[1,3] Jin Chen,[1] Margarida Barroso,[2] and Xavier Intes[1,*]

[1]*Department of Biomedical Engineering, Rensselaer Polytechnic Institute, 110 8th Street, Troy, New York. 12180, USA*

[2]*Center for Cardiovascular Sciences, Albany Medical College, 43 New Scotland Avenue, Albany, New York, 12208, USA*

[3]*Currently with the Center for Molecular Imaging, Beth Israel Deaconess Medical Center, 330 Brookline Avenue, Boston, Massachusetts 02215, USA*

*intesx@rpi.edu

Abstract: Forster resonance energy transfer (FRET) is a nonradiative transfer of energy between two fluorescent molecules (a donor and an acceptor) in nanometer range proximity. FRET imaging methods have been applied to proteomic studies and drug discovery applications based on intermolecular FRET efficiency measurements and stoichiometric measurements of FRET interaction as quantitative parameters of interest. Importantly, FRET provides information about biomolecular interactions at a molecular level, well beyond the diffraction limits of standard microscopy techniques. The application of FRET to small animal imaging will allow biomedical researchers to investigate physiological processes occurring at nanometer range in vivo as well as in situ. In this work a new method for the quantitative reconstruction of FRET measurements in small animals, incorporating a full-field tomographic acquisition system with a Monte Carlo based hierarchical reconstruction scheme, is described and validated in murine models. Our main objective is to estimate the relative concentration of two forms of donor species, i.e., a donor molecule involved in FRETing to an acceptor close by and a nonFRETing donor molecule.

References and links

1. B. Huang, M. Bates, and X. Zhuang, "Super-resolution fluorescence microscopy," Annu. Rev. Biochem. **78**(1), 993–1016 (2009).
2. L. Stryer, "Fluorescence energy transfer as a spectroscopic ruler," Annu. Rev. Biochem. **47**(1), 819–846 (1978).
3. E. A. Jares-Erijman and T. M. Jovin, "Imaging molecular interactions in living cells by FRET microscopy," Curr. Opin. Chem. Biol. **10**(5), 409–416 (2006).
4. A. Miyawaki, J. Llopis, R. Heim, J. M. McCaffery, J. A. Adams, M. Ikura, and R. Y. Tsien, "Fluorescent indicators for Ca2+ based on green fluorescent proteins and calmodulin," Nature **388**(6645), 882–887 (1997).
5. M. Mank, D. F. Reiff, N. Heim, M. W. Friedrich, A. Borst, and O. Griesbeck, "A FRET-based calcium biosensor with fast signal kinetics and high fluorescence change," Biophys. J. **90**(5), 1790–1796 (2006).
6. H. Ueyama, M. Takagi, and S. Takenaka, "A novel potassium sensing in aqueous media with a synthetic oligonucleotide derivative. Fluorescence resonance energy transfer associated with Guanine quartet-potassium ion complex formation," J. Am. Chem. Soc. **124**(48), 14286–14287 (2002).
7. T. Kuner and G. J. Augustine, "A genetically encoded ratiometric indicator for chloride: capturing chloride transients in cultured hippocampal neurons," Neuron **27**(3), 447–459 (2000).
8. N. Mochizuki, S. Yamashita, K. Kurokawa, Y. Ohba, T. Nagai, A. Miyawaki, and M. Matsuda, "Spatio-temporal images of growth-factor-induced activation of Ras and Rap1," Nature **411**(6841), 1065–1068 (2001).
9. A. Nezu, A. Tanimura, T. Morita, A. Shitara, and Y. Tojyo, "A novel fluorescent method employing the FRET-based biosensor "LIBRA" for the identification of ligands of the inositol 1,4,5-trisphosphate receptors," Biochim. Biophys. Acta **1760**(8), 1274–1280 (2006).
10. T. Nishioka, K. Aoki, K. Hikake, H. Yoshizaki, E. Kiyokawa, and M. Matsuda, "Rapid turnover rate of phosphoinositides at the front of migrating MDCK cells," Mol. Biol. Cell **19**(10), 4213–4223 (2008).

11. I. T. Li, E. Pham, and K. Truong, "Protein biosensors based on the principle of fluorescence resonance energy transfer for monitoring cellular dynamics," Biotechnol. Lett. **28**(24), 1971–1982 (2006).
12. S. Kumar, D. Alibhai, A. Margineanu, R. Laine, G. Kennedy, J. McGinty, S. Warren, D. Kelly, Y. Alexandrov, I. Munro, C. Talbot, D. W. Stuckey, C. Kimberly, B. Viellerobe, F. Lacombe, E. W.-F. Lam, H. Taylor, M. J. Dallman, G. Stamp, E. J. Murray, F. Stuhmeier, A. Sardini, M. Katan, D. S. Elson, M. A. A. Neil, C. Dunsby, and P. M. W. French, "FLIM FRET technology for drug discovery: automated multiwell-plate high-content analysis, multiplexed readouts and application in situ," ChemPhysChem **12**(3), 609–626 (2011).
13. J. R. Lakowicz and B. R. Masters, "Principles of fluorescence spectroscopy, third edition," J. Biomed. Opt. **13**(2), 029901 (2008).
14. H. Wallrabe and A. Periasamy, "Imaging protein molecules using FRET and FLIM microscopy," Curr. Opin. Biotechnol. **16**(1), 19–27 (2005).
15. B. Breart, F. Lemaître, S. Celli, and P. Bousso, "Two-photon imaging of intratumoral CD8+ T cell cytotoxic activity during adoptive T cell therapy in mice," J. Clin. Invest. **118**(4), 1390–1397 (2008).
16. J. McGinty, H. B. Taylor, L. Chen, L. Bugeon, J. R. Lamb, M. J. Dallman, and P. M. W. French, "In vivo fluorescence lifetime optical projection tomography," Biomed. Opt. Express **2**(5), 1340–1350 (2011).
17. C. Vinegoni, C. Pitsouli, D. Razansky, N. Perrimon, and V. Ntziachristos, "In vivo imaging of Drosophila melanogaster pupae with mesoscopic fluorescence tomography," Nat. Methods **5**(1), 45–47 (2008).
18. V. Ntziachristos, J. Ripoll, L. V. Wang, and R. Weissleder, "Looking and listening to light: the evolution of whole-body photonic imaging," Nat. Biotechnol. **23**(3), 313–320 (2005).
19. V. Gaind, K. J. Webb, S. Kularatne, and C. A. Bouman, "Towards in vivo imaging of intramolecular fluorescence resonance energy transfer parameters," J. Opt. Soc. Am. A **26**(8), 1805–1813 (2009).
20. V. Gaind, S. Kularatne, P. S. Low, and K. J. Webb, "Deep-tissue imaging of intramolecular fluorescence resonance energy-transfer parameters," Opt. Lett. **35**(9), 1314–1316 (2010).
21. J. McGinty, D. W. Stuckey, V. Y. Soloviev, R. Laine, M. Wylezinska-Arridge, D. J. Wells, S. R. Arridge, P. M. W. French, J. V. Hajnal, and A. Sardini, "In vivo fluorescence lifetime tomography of a FRET probe expressed in mouse," Biomed. Opt. Express **2**(7), 1907–1917 (2011).
22. A. K. Kenworthy and M. Edidin, "Distribution of a glycosylphosphatidylinositol-anchored protein at the apical surface of MDCK cells examined at a resolution of <100 A using imaging fluorescence resonance energy transfer," J. Cell Biol. **142**(1), 69–84 (1998).
23. H. Wallrabe, Y. Chen, A. Periasamy, and M. Barroso, "Issues in confocal microscopy for quantitative FRET analysis," Microsc. Res. Tech. **69**(3), 196–206 (2006).
24. S. Padilla-Parra, N. Audugé, M. Coppey-Moisan, and M. Tramier, "Quantitative FRET analysis by fast acquisition time domain FLIM at high spatial resolution in living cells," Biophys. J. **95**(6), 2976–2988 (2008).
25. M. J. Niedre, R. H. de Kleine, E. Aikawa, D. G. Kirsch, R. Weissleder, and V. Ntziachristos, "Early photon tomography allows fluorescence detection of lung carcinomas and disease progression in mice in vivo," Proc. Natl. Acad. Sci. U.S.A. **105**(49), 19126–19131 (2008).
26. J. Chen, V. Venugopal, and X. Intes, "Monte Carlo based method for fluorescence tomographic imaging with lifetime multiplexing using time gates," Biomed. Opt. Express **2**(4), 871–886 (2011).
27. V. Venugopal, J. Chen, and X. Intes, "Development of an optical imaging platform for functional imaging of small animals using wide-field excitation," Biomed. Opt. Express **1**(1), 143–156 (2010).
28. C. Chang and M. Mycek, "Improving precision in time-gated FLIM for low-light live-cell imaging," in *Molecular Imaging II*, K. Licha and C. Lin, eds., Vol. 7370 of Proceedings of SPIE-OSA Biomedical Optics (Optical Society of America, 2009), paper 7370_09.
29. S. Bélanger, M. Abran, X. Intes, C. Casanova, and F. Lesage, "Real-time diffuse optical tomography based on structured illumination," J. Biomed. Opt. **15**(1), 016006 (2010).
30. J. Chen, V. Venugopal, F. Lesage, and X. Intes, "Time-resolved diffuse optical tomography with patterned-light illumination and detection," Opt. Lett. **35**(13), 2121–2123 (2010).
31. J. Chen and X. Intes, "Time-gated perturbation Monte Carlo for whole body functional imaging in small animals," Opt. Express **17**(22), 19566–19579 (2009).
32. N. Valim, J. Brock, and M. Niedre, "Experimental measurement of time-dependent photon scatter for diffuse optical tomography," J. Biomed. Opt. **15**(6), 065006 (2010).
33. A. H. Hielscher, R. E. Alcouffe, and R. L. Barbour, "Comparison of finite-difference transport and diffusion calculations for photon migration in homogeneous and heterogeneous tissues," Phys. Med. Biol. **43**(5), 1285–1302 (1998).
34. K. M. Yoo, F. Liu, and R. R. Alfano, "When does the diffusion approximation fail to describe photon transport in random media?" Phys. Rev. Lett. **64**(22), 2647–2650 (1990).
35. J. Chen and X. Intes, "Mesh-based Monte Carlo method in time-domain widefield fluorescence molecular tomography," J. Biomed. Opt. **17**(10), 106009 (2012).
36. S. R. Arridge and W. R. B. Lionheart, "Nonuniqueness in diffusion-based optical tomography," Opt. Lett. **23**(11), 882–884 (1998).
37. A. Soubret, J. Ripoll, and V. Ntziachristos, "Accuracy of fluorescent tomography in the presence of heterogeneities: study of the normalized Born ratio," IEEE Trans. Med. Imaging **24**(10), 1377–1386 (2005).
38. V. Ntziachristos and R. Weissleder, "Experimental three-dimensional fluorescence reconstruction of diffuse media by use of a normalized Born approximation," Opt. Lett. **26**(12), 893–895 (2001).

39. P. J. Verveer, A. Squire, and P. I. Bastiaens, "Global analysis of fluorescence lifetime imaging microscopy data," Biophys. J. **78**(4), 2127–2137 (2000).
40. N. A. Rahim, S. Pelet, R. D. Kamm, and P. T. C. So, "Methodological considerations for global analysis of cellular FLIM/FRET measurements," J. Biomed. Opt. **17**(2), 026013 (2012).
41. R. Cubeddu, A. Pifferi, P. Taroni, A. Torricelli, and G. Valentini, "Time-resolved imaging on a realistic tissue phantom: μ(s)' and μ(a) images versus time-integrated images," Appl. Opt. **35**(22), 4533–4540 (1996).
42. J. Chen and X. Intes, "Comparison of Monte Carlo methods for fluorescence molecular tomography-computational efficiency," Med. Phys. **38**(10), 5788–5798 (2011).
43. S. B. Raymond, D. A. Boas, B. J. Bacskai, and A. T. N. Kumar, "Lifetime-based tomographic multiplexing," J. Biomed. Opt. **15**(4), 046011 (2010).
44. M. Y. Berezin, K. Guo, W. Akers, R. E. Northdurft, J. P. Culver, B. Teng, O. Vasalatiy, K. Barbacow, A. Gandjbakhche, G. L. Griffiths, and S. Achilefu, "Near-infrared fluorescence lifetime pH-sensitive probes," Biophys. J. **100**(8), 2063–2072 (2011).
45. N. Gaborit, C. Larbouret, J. Vallaghe, F. Peyrusson, C. Bascoul-Mollevi, E. Crapez, D. Azria, T. Chardès, M.-A. Poul, G. Mathis, H. Bazin, and A. Pèlegrin, "Time-resolved fluorescence resonance energy transfer (TR-FRET) to analyze the disruption of EGFR/HER2 dimers: a new method to evaluate the efficiency of targeted therapy using monoclonal antibodies," J. Biol. Chem. **286**(13), 11337–11345 (2011).
46. A. Periasamy, H. Wallrabe, Y. Chen, and M. Barroso, "Quantitation of protein–protein interactions: confocal FRET microscopy," in *Biophysical Tools for Biologists, Volume Two,* Vol. 89 of Methods in Cell Biology (Academic, 2008), pp. 569–598.
47. H. Li and Z. M. Qian, "Transferrin/transferrin receptor-mediated drug delivery," Med. Res. Rev. **22**(3), 225–250 (2002).

1. Introduction

Fluorescence is a widely used readout of molecular localization that has enabled the elucidation of many biological processes. Co-localization of different fluorophores via fluorescence microscopy cannot monitor nanometer range proximity between proteins due to the resolution limits of the imaging technique. Although super-resolved imaging microscopy techniques [1] can break the diffraction limit, it is not currently applicable to the imaging of protein-protein interactions in live cells or tissues. Forster Resonance energy transfer (FRET) is routinely used as nanometer range proximity based assay to sense protein-protein interactions in live cells. FRET is the radiationless transfer of energy from an excited donor fluorophore to an appropriate acceptor in close proximity. The energy transfer only occurs between fluorophores separated by less than ~10 nm allowing the detection of protein interactions at the nano-scale [2,3]. As well as being used to detect intermolecular interactions between appropriately labeled proteins, either as an end point in fixed cells or as a dynamic process in live cells, FRET is also utilized in a range of genetically expressed intracellular biosensors of which the cameleon calcium sensor is the first and best known [4]. A wide array of intramolecular FRET biosensors are available to sense, for example, calcium [5], potassium [6], chloride [7], GTP [8], IP3 [9], PIP2 [10] and others [11]. While FRET has been extensively applied in the nondestructive assessment of molecular phenomena in cell-based assays, it is becoming increasingly important to translate FRET assays to detect intra- as well as intermolecular interactions to small animal imaging where the in vivo physiological context is critical for drug development, the study of diseases, and fundamental cellular and molecular biology [12].

FRET sensing is based on the detection of the reduction in the intensity level and fluorescence lifetime of the donor signal or of the increase in acceptor signal (sensitized emission) upon energy transfer from donor to acceptor fluorophore [13]. Lifetime-based imaging methods, namely fluorescence lifetime imaging microscopy (FLIM), provide a quantitative estimation of FRET activity through the measurement of the fluorescence decay of the donor signal, requiring only the measurement of the donor lifetime signal. FLIM-FRET methods provide a highly robust approach to measure FRET due to the invariance of fluorescence lifetime with fluorophore concentration, excitation intensity and other experimental parameters [14]. Several FRET imaging techniques have been applied to small animal models. For example, one of these approaches employs intravital microscopy using two-photon microscopes [15]. However these methods are confined to the assessment of

superficial tissue due to the limited penetration of light into biological tissue. Alternatively, mesoscopic imaging methods which allow tomographic imaging of fluorescence (e.g., optical projection tomography) have been employed for FRET imaging [12,16]. Such techniques are however restricted to relatively thin samples (2–3 mm thick) due to the highly scattering propagation of photons in biological tissue [17]. Therefore, macroscopic imaging methods based in the diffuse regime, which rely on rigorous mathematical models of photon propagation and measurement of multiple projections across the model (for instance fluorescence molecular tomography (FMT)) must be used for small animal imaging [18].

Classical FRET imaging techniques for in vivo applications have been limited to the detection of intramolecular FRET interactions using genetically expressed biosensor constructs [19–22]. Intramolecular FRET (occurring between donor and acceptor fluorophores on the same host molecule) is straightforward to detect, analyze and interpret due to the presence of fixed acceptor-donor ratios (A:D) ratios. However, these approaches rely on FRET pairs excited and emitting in the visible spectral range. Hence, FRET imaging in preclinical models is still confined to the investigation of relatively small volumes (limbs for instance) due to the reduced penetration of light emitted by FRET-pairs in the visible spectrum through tissue [16,21]. Due to the lack of genetically expressed FRET pairs in the NIR, it is necessary to employ FRET-compatible organic dye fluorophores in the NIR spectral range to perform whole-body FRET imaging in preclinical models.

Intermolecular FRET, i.e., protein-protein interactions between donor-labeled and acceptor-labeled proteins, either soluble or associated with membranes can be detected by using genetically expressed fluorescence proteins fused to the target protein pair of interest. Furthermore, intermolecular FRET can also be detected via labeling of donor- and acceptor-labeled ligands or anti-extracellular domain antibodies added extracellularly to allow for binding to dimerized/oligomerized surface receptors. Conversely to intramolecular FRET, intermolecular FRET efficiency is directly related to the acceptor-donor ratios (A:D). As shown previously, intermolecular FRET is linearly dependent on A:D ratios due to specific protein-protein interactions that result in the formation of protein complexes; with higher acceptor-donor ratios resulting in higher FRET signals [23]. In cell-based assays employing intermolecular FRET interaction, the fluorophore pairs are typically conjugated to soluble ligands, e.g., EGF, transferrin and others, that can come into nanometer-range FRET proximity upon binding to their dimerized/oligomerized respective receptors. The translation of such techniques to preclinical models holds tremendous potential for investigation of cancer biology and drug development.

Here we report on the use of a new tomographic imaging technique for whole-body small animal intermolecular NIR FRET imaging. Our approach to FRET imaging in small animal models relies on the existence of two donor fluorophore states, one in which the donor fluorophore will be in proximity to the acceptor (FRETing donor) and another where the donor fluorophore does not experience FRET (nonFRETing donor). This approach is well suited to detect intermolecular protein-protein interactions which are crucial to many physiologically significant cellular processes. The binding of donor-labeled protein to its acceptor-labeled interacting partner inherently assumes the existence of two donor species one engaged in FRET and another that is not engaged in FRET due to presence of multiple and diverse A:D ratios. As stated above, the FRETing donor molecule will exhibit a shorter fluorescence lifetime when compared to the nonFRETing donor. Therefore, the quantification of FRET activity resumes to the quantitative unmixing of two fluorophores (donor states) with fluorescence lifetime contrast and potentially spatially co-localized. The derivation of quantitative metrics in FLIM-FRET techniques can thus be cast on the estimation of four parameters—the relative contributions and lifetimes of each donor species [24]. The translation of FLIM-based FRET detection methods to the macroscopic imaging regime is done using time-resolved FMT [21]. The principle of time resolved FMT is based on the measurement of photons exiting the animal model over time (usually over a few ns) upon the

injection of an ultra-short laser pulse into the animal model. This measurement data type referred to as the temporal point spread function (TPSF) provides a wealth of information for tomographic reconstruction of fluorescent markers in thick tissue. For instance, the use of minimally scattered photons measured on the rising portion of the TPSF provides an approach towards improvement in the low resolution performance (inherent to diffuse imaging methods) [25]. Furthermore, the decaying portion of the TPSF encodes the contrast in fluorescent lifetime of the FRETing and nonFRETing donors which can be used to quantitatively estimate their relative concentrations in vivo [26]. Hence, combining measurements spanning both the early rising and decaying portion of the TPSF in the inverse problem provide sufficient tomographic information to quantitatively localize FRET activity in preclinical models with relatively high-resolution. However, the acquisition of such spatially and temporally dense data sets using classical tomographic imaging paradigms results in prohibitive acquisition times when employed for whole-body preclinical imaging studies. In this work, we combine four novel and unique approaches in optical tomography imaging to mitigate the limitations of time-resolved whole-body imaging thus allowing one to accurately estimate these parameters in vivo in small animal models. First, we implement a time-resolved imaging platform based on a wide-field excitation paradigm which allows the fast acquisition of temporally dense data sets over the whole body of the small animal model. Second, a Monte Carlo based mathematical model is implemented to reconstruct the concentrations of the two donor species using the time gate data type. Furthermore, a hierarchical inversion scheme is implemented, which allows the efficient combination of complementary information provided by the early (resolution) and late time gates (quantification/unmixing) data type. And lastly, we report the use of an intermolecular FRET antibody-antigen FRET pair compatible fluorophore pair which emits in the Near-Infrared (NIR) window. The fluorophore characterization and tomographic studies presented herein demonstrate an accurate quantification of intermolecular FRET activity in vivo in small animal murine models.

2. Methods and materials

2.1. Imaging system

The tomographic imaging platform employed in this study employs a wide-field illumination imaging wherein a pulsed laser source spanning a region of interest (described below) is projected on the model and the temporal measurements exiting the animal model in transmittance are acquired using a time-gated intensified CCD camera [27]. In the experiments described herein, the body of the mouse model (from neck to tail) is selected as the region of interest. The use of patterned excitation coupled with wide-field detection allows the measurement of photons with high spatial density. It is also worth noting that the excitation scheme can be easily scaled to match the region of interest allowing the investigation of extended volumes. The reduction in number of source measurements employed when using wide-field illumination compared to point-based illumination, permits the fast acquisition of tomographic measurements spanning the whole body as well as the acquisition of dense temporal measurements within a few minutes. Furthermore, the wide-field excitation scheme injects a larger number of photons into the model thereby ensuring improved signal-to-noise ratio while maintaining the incident photon intensity well within the maximum permissible exposure limits. These characteristics of the system provide an important advantage in whole-body FRET tomography where the quantitative accuracy of the method critically depends on the robustness of the measurements in the spatial and temporal domain [28].

The design of the time-resolved imaging system used in this study is shown in Fig. 1a and is described in detail in [27]. Briefly, the platform incorporates a tunable Ti:sapphire laser (Mai Tai HP, Spectra-Physics, USA) used in conjunction with a closed loop power control
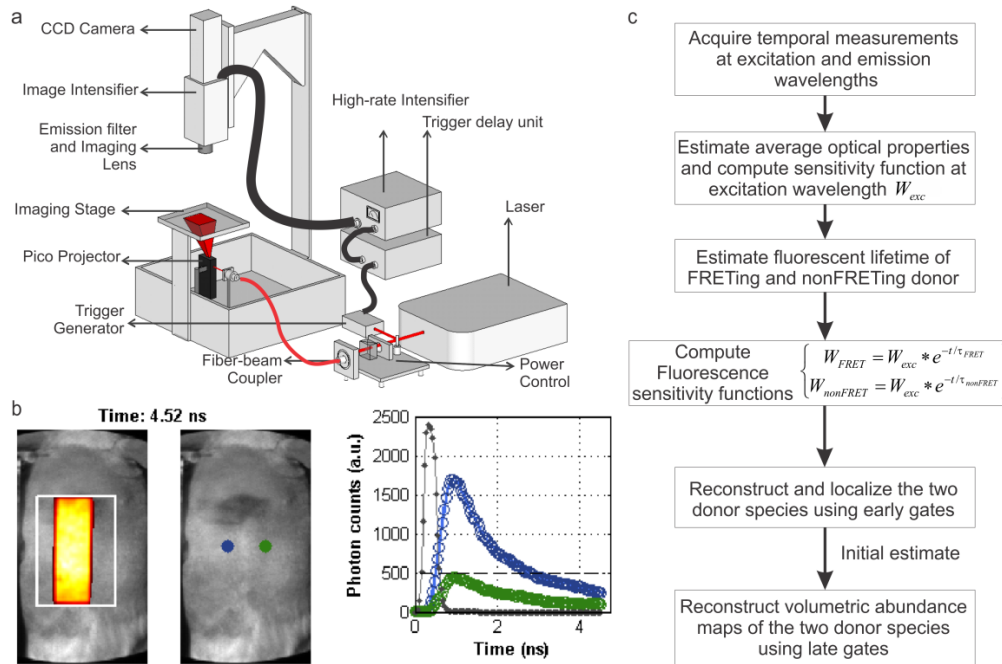
Fig. 1. a, Schematic of the tomographic imaging platform. b, Excerpt from video showing imaging protocol for wide-field time-resolved tomography (Media 1) c, Hierarchical reconstruction scheme flowchart.

system (providing up to 1.8 W power at 800 nm). During mode-locked operation the laser generates 100 fs pulses at 80 MHz repetition rate (allowing a maximum measurement window of 12.5 ns) and is tunable from 690–1020 nm. The output from the power control module is guided to a spatial light modulator which generates the patterns using a 400μm optical fiber (0.22 NA). The wide-field excitation patterns are produced using a modified pico projector module (Optoma PK101) wherein the in-built RGB LED light source in the projector is replaced by the output from the laser using a beam focuser. The pico projector allows the easy implementation of complex user generated patterns (via a USB connection through PowerPoint) with a compact light engine in the module. The temporal measurements of photons exiting the surface of the animal, referred to as the Temporal Point Spread Function (TPSF), are made using a gated Intensified CCD (ICCD) camera (Picostar HR, LaVision GmbH, Germany). The image intensifier component of the camera allows the acquisition of gated measurements which refers to the total number of photons recorded over a fixed time when the gate is open. This ICCD can be operated on gatewidths ranging from 200–000 ps. The signal amplification of the recorded measurements can be controlled at the image intensifier by modifying the voltage applied across the cathode tube in the intensifier (260 V – 800 V). The CCD camera has a resolution of 1376 x 1040 pixels and is focused on the imaging stage using a Nikon 50 mm f/1.8D AF Nikkor Lens. The recorded CCD images are hardware binned (4 x 4) to record images over a 65 x 86 mm region at a resolution of 0.25 mm/pixel. The fluorescence measurements are acquired using discrete filter sets (Semrock, USA).

The full-field pattern projected on the stage spanned a 32 x 25 mm^2 region of interest. The spatial and temporal characteristics of the pattern were measured by directly imaging the time-resolved signal on a white diffusing paper placed on the stage. The intensity of photons incident on the stage have a nonuniform distribution across the region of interest due to nonlinearities in the projector optics. Furthermore, the temporal characteristics of the pattern projected on the stage was observed to have a spatially dependent variation of 80 ps (Full-

width-at-half-maximum) and 40 ps (time of arrival). These spatial and temporal variations necessitate the inclusion of the pattern characteristics and IRF in the reconstruction scheme.

2.2. Imaging protocol

In the studies described herein, a set of bar-shaped patterns are selected as the wide-field illumination scheme [29,30]. The patterns are defined such that for any pattern, half of the imaging area along the x-axis or the y-axis is uniformly illuminated. These patterns are then shifted along the corresponding axis at fixed separation providing the set of excitation patterns. These studies employed a total of 36 patterns, with 18 patterns along each axis. The execution of the above described illumination process is shown in the movie (Media 1, Fig. 1b). For all experiments described herein, the excitation wavelength was set at 695 nm and the emission wavelength was set at 720 nm. Furthermore, the gatewidth on the ICCD camera was set to 400 ps. The excitation signals were collected over a 2 ns time window at 40 ps resolution (50 gates) with the integration time of the camera set to 25 ms and the MCP voltage of 600 V. The measurements at the excitation wavelength for the complete set were acquired in 3 min. The fluorescence signals were recorded over a 5 ns time window at 40 ps resolution (125 gates) with the integration time of 640 ms and MCP voltage of 600 V. The emission measurements for all patterns were acquired in 34 minutes.

Following the optical imaging protocol, the samples were imaged on a microCT platform (VivaCT40, Scanco) to obtain a volumetric map of the models for validation of the tomographic localization using this method. The CT images were acquired at an isotropic resolution of 38μm. It should be noted that the 3D volume acquired on the CT was only used to extract the surface information for complex boundary encountered in the mouse model which was used in the calculation of the homogeneous weight matrix incorporating no anatomical markers.

2.3. Reconstruction scheme

Another equally important aspect of tomographic imaging is the accuracy of the photon propagation model employed to describe the transport of photons in biological tissue. This becomes especially significant when employing time-resolved data sets where the transport of early photons is not accurately modeled by classical deterministic schemes based on the Radiative Transport Equation or its approximation, the Diffusion Equation (DE) [31,32]. Moreover, the wide range of optical properties encountered when performing whole-body imaging studies in small animal models necessitate the use of a stochastic photon propagation model [33,34]. Herein, we employ a Monte Carlo based propagation model which can accurately model the temporal response of the tissue across all time points in the typical measurement window (including minimally scattered early photons) [26,35]. The propagation model establishes a relationship (referred to as weight functions) between the excitation source and the measurement collected by the emission detector, based on the model geometry and optical properties. This model is then used to reconstruct the fluorophore concentration in vivo by solving a highly ill-posed inverse problem [36]. In order to reconstruct the parameters quantifying the FRET interaction using time-resolved data types, the weight functions obtained using the propagation model are convolved by the lifetimes of the FRETing and nonFRETing donor fluorophores [26].

The photon propagation model used for FMT closely follows the perturbation Monte Carlo model described for functional tomography [26,31]. Here we define the total absorption coefficients due to the background tissue and fluorophores as μ_a^x and μ_a^m at the excitation wavelength (λ_x) and emission wavelength (λ_m), respectively. Then the effective quantum yield $\eta(r)$ is defined as the probability of a photon to be emitted upon absorption of a photon by the total absorption coefficient,

$$\eta(r) = \frac{\mu_{af}^x(r)\phi}{\mu_a^x(r)} \tag{1}$$

where φ is the quantum yield and μ_{af}^{x} is the absorption coefficient contributed by the fluorophore, which is linearly related to the concentration of the fluorophore by the extinction coefficient. For a fluorophore in the medium that has a mono-exponential decay with lifetime τ, under the assumption of equal absorption and scattering coefficients at λ_x and λ_m, the fluorescence signals can be simulated by convolving the temporal signals generated at the excitation wavelength by the exponential time decay of the fluorophore given by $\exp(-t/\tau)$. The spatial and temporal jacobians for FMT can therefore be calculated using the weight matrices computed for functional tomography ($W^a(t)$)using the following:

$$W^{fluo}(t) = \int_0^t dt' W^a(t') e^{-(t-t')/\tau} \tag{2}$$

Using the lifetime values estimated for the FRETing and nonFRETing donor species, we can therefore construct the weight functions for each FRET complex component ($W^{FRET}(t)$ and $W^{nonFRET}(t)$). It should be noted that for wide-field optical tomography the calculation of $W^a(t)$ simulates the broad uniform excitation patterns by injecting photons with uniform probability across the prescribed area of excitation. Furthermore, in order to account for nonuniform intensity distribution across the experimental excitation patterns the injected photons are weighted by the corresponding intensity level on the measured excitation pattern. This ensures the accurate simulation of photon propagation conditions observed in the experimental settings.

To cast the inverse problem, we employed a Born formulation in which the emission field is normalized by the excitation field [37,38]. Herein, the experimental time-domain emission measurements are normalized by the CW excitation flux at the same position. We therefore have

$$\Phi = \frac{M_i^m(t)}{M_i^x} = \frac{\alpha}{U_i^x}\left[\int d^3r W_i^{FRET}(t)\eta^{FRET} + \int d^3r W_i^{nonFRET}(t)\eta^{nonFRET}\right] \tag{3}$$

where α incorporates gain and attenuation factors employed during measurement acquisition (change in power, and integration time), $M_i^m(t)$ is the total signal from all fluorophores with different lifetimes at the emission wavelength for the ith pattern-detector pair at time-gate t, M_i^x and U_i^x are the measured and simulated total excitation flux measured at the detector for the ith pattern-detector pair respectively. This normalization efficiently mitigates the dependence of the detected fluorescent signal on the optical properties of the examined tissue and thus the absorptive heterogeneities associated with the different organs in the small animal model are not modeled. Note also that this formulation employs the CW excitation flux at the same position to alleviate the unavoidable temporal errors associated with drift and jitter in time-resolved studies. For a reconstruction problem involving K pattern-detector pairs, 2 fluorophore species (FRETing and nonFRETing donor) and a model discretized into J voxels, the above equation can be written as the linear system

$$\begin{bmatrix} \Phi_1 \\ \vdots \\ \Phi_K \end{bmatrix} = \begin{bmatrix} \beta_1 W_{1,1}^{FRET} & \cdots & \beta_1 W_{1,J}^{FRET} & \beta_1 W_{1,1,}^{nonFRET} & \cdots & \beta_1 W_{1,J}^{nonFRET} \\ \vdots & \ddots & \vdots & \vdots & \ddots & \vdots \\ \beta_K W_{K,1}^{FRET} & \cdots & \beta_K W_{K,J}^{FRET} & \beta_K W_{K,1}^{nonFRET} & \cdots & \beta_K W_{K,J}^{nonFRET} \end{bmatrix} \begin{bmatrix} \eta_1^{FRET} \\ \vdots \\ \eta_J^{FRET} \\ \eta_1^{nonFRET} \\ \vdots \\ \eta_J^{nonFRET} \end{bmatrix} \tag{4}$$

Here $W_{i,j}^{FRET}$ and $W_{i,j}^{nonFRET}$ are the weight functions for the ith ($i = 1, ..., K$) measurement and the FRETing and nonFRETing donor species respectively. $\beta_i = \alpha_i/U_i^x$ is the normalization factor for the ith measurement and the corresponding weight function. The above equation has a general form $Ax = b$, and the distribution of the FRETing and nonFRETing donors, x = $[\eta_1^{FRET}, ..., \eta_J^{FRET}, \eta_1^{nonFRET}, ..., \eta_J^{nonFRET}]^{T}$ is computed by solving the above system using a least-squares solver, *lsqr* (MATLAB, MathWorks, USA).

As mentioned previously, the time-gates can be broadly classified into two groups around the maximum gate—early gates and late gates. While a typical temporal measurement can provide measurements at up to 125 time gates, the use of all gates when solving the inverse problem in Eq. (4) is impractical due to computational and memory constraints. Therefore, in this work we implement a hierarchical reconstruction scheme where the effective quantum yield is reconstructed in two steps (Fig. 1c). Once the weight functions are computed for all time gates in the measurements, the reconstruction process is carried out using the following approach. First, the fluorescence signal is localized in 3D using photon measurements at early gates allowing a higher resolution localization of the fluorescence distribution. The distribution thus obtained is used as the initial estimate for the second reconstruction step using measurements spanning the decaying portion of the fluorescence signal. The late gates encoding the contrast in lifetime therefore provide the quantitative estimate of relative abundances of the two species in the volume investigated. In the studies described in this work, one early gate at 50% of the maximum on the rising portion of the TPSF was used for the first step. The second reconstruction step employed 4 gates spanning the fluorescence signal on the decaying portion of the TPSF at 100%, 80%, 60% and 40%. It is worth noting that gates are selected based on the fluorescence signal derived from the detector with maximum signal count in order to mitigate effects of lower signal-to-noise ratio on the reconstruction performance.

2.4. Lifetime estimation using bi-exponential fluorescence decay model

An important aspect of the above method is that the lifetimes of the donor species are assumed to be constant which reduces the ill-posedness of the inverse problem (which is more significant when simultaneously reconstructing multiple parameters). This approach is similar to the Global Lifetime analysis technique employed in FLIM-FRET studies [39,40]. The above assumption makes the accurate estimation of FRETing and nonFRETing donor lifetimes an important factor in the quantitative accuracy of the method. In this work, the lifetime distribution of the FRET-complex components was analyzed using a bi-exponential decay model wherein we estimated 4 unknown parameters – lifetimes and relative abundances of the FRETing and nonFRETing component of the donor molecules in the sample. For the temporal fluorescence decay function $\Gamma_{em}(t)$, recorded in the absence of a diffusing medium on a system with instrument function response IRF(t), the biexponential decay model is given by

$$\Gamma_{em}(t) = IRF(t) * (N + A_{FRET}e^{-t/\tau_{FRET}} + A_{nonFRET}e^{-t/\tau_{nonFRET}}) \qquad (5)$$

Here A_{FRET} and $A_{nonFRET}$ are the relative amplitudes, τ_{FRET} and $\tau_{nonFRET}$ are the lifetime values for the two species. Also, N is an arbitrary additive factor introduced to account for the noise in the TPSF. It should be noted that temporal measurements acquired in transmittance through the model are modified by the tissue transfer function (dependent on the optical properties). In order to mitigate the effect of optical properties in such cases, we replace the IRF in Eq. (5), by the temporal measurement at the excitation wavelength at the corresponding detector which accurately incorporates the effect of optical properties into the model. The measured fluorescence decay (from 99% to 1% of peak intensity) is fit to this model and the above four parameters are estimated using a nonlinear constrained minimization method based on sequential quadratic programming, *fmincon* (MATLAB, MathWorks, USA).

3. NIR FRET pair

The high absorption of visible photons transmitted through biological tissue necessitates the use of a FRET-compatible fluorophore pair in the NIR range (650 nm to1000 nm) owing to the maximum transmission of photons in this spectral window. It is worth noting that the use of NIR FRET pair in small animal models also mitigates any interference due to tissue autofluorescence. Among commercially available fluorophores two Alexa Fluor dyes, Alexa Fluor 700 (donor) and Alexa Fluor 750 (acceptor) (Life techonologies, Inc), are suitable for FRET imaging in the NIR wavelengths due to the significant spectral overlap of their donor emission and acceptor excitation spectra (Fig. 2a). Moreover, the Forster distance for this fluorophore pair was found to be 7.76 nm (comparable to existing FRET pairs [2]), which ensured that the donor molecule will transfer energy to the acceptor molecule with high probability at distances relevant for biological applications. The FRET compatibility of the two NIR fluorophores was investigated using functionalized variants of Alexa Fluor 700 and Alexa Fluor 750; Alexa Fluor 700 Mouse IgG1 (MG129, Invitrogen, CA, USA) and Alexa Fluor 750 goat anti-mouse IgG (A21037, Invitrogen, CA, USA). This antibody-antigen pair is an excellent model to study specific intermolecular interactions as detected by NIR FRET. In order to construct 5 samples with varying acceptor-to-donor (AD) ratio; first the donor stock sample was diluted to concentration of 20μg/ml using Phosphate Buffered Saline (PBS) as the buffer. Similarly, the acceptor stock sample was diluted to two 500μl samples having concentrations of 20μg/ml and 80μg/ml. Next, 5 200μl aliquots of the donor were prepared and different volumes of the acceptor samples and PBS were added to obtain AD ratios of 0.25, 0.5, 1, 2 and 4 with a final donor concentration of 10μg/ml. The samples were incubated for 5 min and subsequently transferred to capillary tubes used in the tomographic studies. As stated previously, the fraction of FRETing donor (f_d) in each sample was expected to linearly increase with the increased acceptor/donor ratios. Capillary tubes containing the above samples were directly imaged (in the absence of any diffusing medium) and the resulting temporal profiles (shown in Fig. 2b) were fit to a biexponential decay model to estimate the baseline lifetimes of the FRETing and nonFRETing donor species.

The characterization of the FRET interaction between the Alexa Fluor dyes comprised of the estimation of the donor (Alexa Fluor 700) lifetime under FRETing and nonFRETing conditions. The degree of reduction in lifetime under FRET plays a critical role in determining the suitability of the Alexa dyes as a FRET-compatible fluorophore pair. This is especially important when selecting dyes for whole body imaging applications where diffused transport of photons can effectively 'smear' the lifetime contrast between the two donor species. It should be noted that the lifetime contrast is significantly higher for mixtures with higher A:D ratios. In order to quantify the temporal characteristics, the TPSF were fit to the bi-exponential decay function and the lifetime of the nonFRETing and FRETing donor molecules were estimated to be 1.1 ± 0.2 ns and 0.29 ± 0.19 ns respectively. The nonFRETing
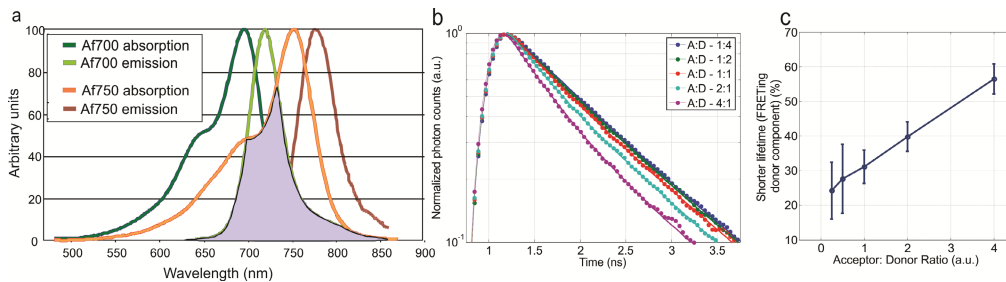

Fig. 2. NIR FRET pair. a, Fluorescence spectra of the Alexa Fluor 700 (donor) and Alexa Fluor 750 (acceptor) dyes. b, Temporal measurements acquired upon direct imaging of multiple mixtures of acceptor and donor fluorophores in varying ratios. c, Fraction of FRETing donor molecules in multiple mixtures with varying Acceptor:Donor (A:D) ratios.

donor lifetime of 1.1 ns is in good agreement with the lifetime of Alexa Fluor 700 dye (as provided by the manufacturer). Furthermore, the fractional amplitude of FRETing donor was found to increase linearly in the five samples from 20% to 60% (Fig. 2c). It should be noted that in this case the fitting procedure was used to estimate the relative concentrations and lifetimes of both donor species to obtain a baseline estimate of all four parameters.

4. Experimental validation

4.1. In vitro validation

We investigated the accuracy of the method in tomographic estimation of f_d in murine models using a 17 mm thick phantom. The tissue mimicking hydro-gel phantom (shown in Fig. 3a) used for the validation of the tomographic estimation method in a homogeneous slab phantom was constructed using agarose (Fluka 05040, Sigma Aldrich, MO, USA). The scattering and absorption coefficients of the phantom were controlled using Titanium Dioxide (Ti-Pure R-101 Titanium Dioxide, DuPont, USA) as the scattering agent and water soluble NIR dye (Epolight 2735, Epolin, USA) as the absorber. Four 10 mm long capillary tubes (1 mm inner diameter) containing the donor-acceptor mixtures with AD ratios of 0.25, 0.5, 2 and 4 were embedded in the phantom at a depth of 11 mm (Fig. 3a). The temporal measurements acquired at the donor excitation and emission wavelengths for each of the 36 patterns were then processed to generate point detector measurements. In this study, 130 detectors at a separation of 3 mm along the x and y axis were employed (Fig. 3b). The optical properties of the phantom were estimated using time-resolved spectroscopy and were found to be, $\mu_a = 0.07$ cm^{-1} and $\mu_s' = 6.17$ cm^{-1} [41]. It should be noted that the optical properties were estimated using the measurements at the above detectors at the excitation wavelength.
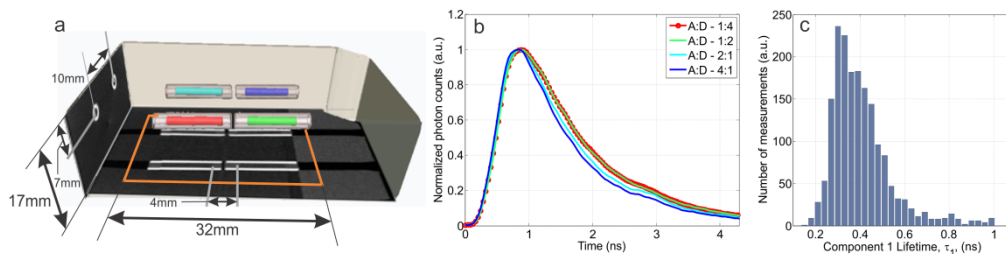

Fig. 3. a, Design of murine phantom with four inclusions carrying mixtures with different acceptor to donor ratios (Red- 1:4, Green-1:2, Cyan-2:1 and Blue-4:1). The orange boundary indicates the area of full-field excitation. b, An example of the normalized temporal measurements acquired at detectors directly above the four inclusions when excited by a full-field excitation pattern. c, Histogram of the value of shorter lifetime (FRETing donor) component for all detectors above signal threshold for all excitation patterns.

Figure 3b shows an example of the normalized temporal measurements acquired at detectors (pixels) directly above the four inclusions. It should be noted that the different capillary tubes exhibit varying lifetimes as observed in Fig. 2b. However, as expected, the lifetime contrast is reduced due to the diffused transport of photons through the phantom. The temporal measurements for all detectors (having maximum photon counts higher than 200 photons) were fit to the biexponential decay model after deconvolution with the excitation signal (to incorporate effects of the optical properties). Figure 3c shows the histogram of the estimated FRETing donor lifetime (Mean estimated lifetime: 0.32 ns, Std. Dev: 0.13 ns).

The results of the hierarchical reconstruction of fluorescence yield of FRETing and nonFRETing donors are shown in Figs. 4(a)–4(b). The 3D visualization (50% iso-volume) of the reconstructed total fluorescence yield (FRETing and nonFRETing donor) obtained following the tomographic reconstruction of the 32 x 40 x 17 mm^3 volume is shown in Fig. 4a. The mean diameter of the 50% iso-volumes of the reconstructed tubes was 6 mm.
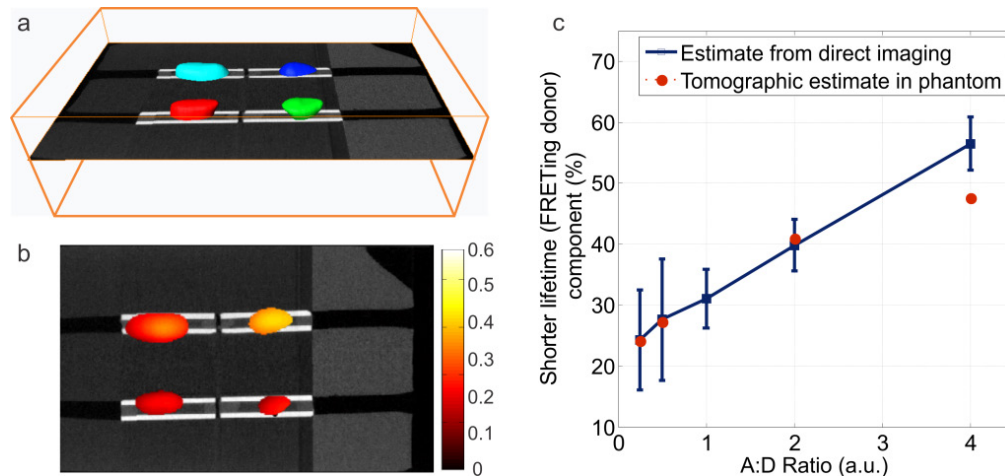
Fig. 4. a, 50% iso volume of total reconstructed fluorescence yield. b, Reconstructed quantum yield of the shorter component thresholded at 50% of maximum value at the slice at depth of 11 mm. c, Quantitative comparison of tomographic estimates of FRETing donor fraction from above reconstruction.

Figure 4b shows the successful resolution of multiple fluorescent inclusions closely situated in a diffusing medium with less than 1 mm error in localization along the x and y axes. The maximum reconstructed quantum yield for the shorter lifetime component (FRETing donor) was used to calculate the estimate of f_d for each object and was used as the performance metric to establish quantitative accuracy. A comparison of the estimated and expected f_d shown in Fig. 4c shows an absolute error of less than 3% in the tomographic estimate for AD ratios less than 2. For AD ratio of 4 the estimation error was found to be higher at 9%.

4.2. Validation in a mouse model

We next investigated the robustness of this method when estimating f_d in a complex optically heterogeneous volume encountered in small animal models. In this study, the small animal model was established using a freshly euthanized mouse (prior to rigor mortis) and localized FRETing conditions were established using capillary tubes implanted in the abdomen. Specifically, the animal body (from neck to tail) was shaved on the dorsal and ventral side and the capillary tubes were inserted into the model through a 5 mm incision in the lower abdomen on the ventral side. The inclusions were attached to the abdominal organs using an optically clear topical tissue adhesive (GLUture, World Precision Instruments, USA). Figure 5a shows the location of the two capillary tubes as obtained from the 3D CT images. It should be noted that the tube with A:D ratio 1:4 is surrounded by the kidneys and the highly absorbing abdominal organs (e.g., liver, spleen and stomach). Conversely, the tube with A:D ratio of 4:1 is located in the relatively optically homogeneous gut region (with significantly lower optical absorption and scattering). The animal model was then placed in an imaging chamber and restrained by mild compression to a thickness of 15 mm. As described in the previous study, the optical properties of the volume investigated were estimated using time-resolved spectroscopy. The reconstruction of fluorescence yield was done using measurements at 171 detectors uniformly distributed across the model (at intervals of 3 mm along the x-axis and 2 mm along the y-axis) for each of the 36 patterns. The feasibility of this approach when imaging complex models was successfully established with the measurement of FRET signal through the mouse model. Figure 5b shows the lifetime contrast in the normalized temporal measurements acquired at point detectors (pixels) approximately above the two capillary tubes. It is worth noting that the lifetime contrast between the two FRET-complexes is retained in the measurements in an optically heterogeneous medium. Figure 5c
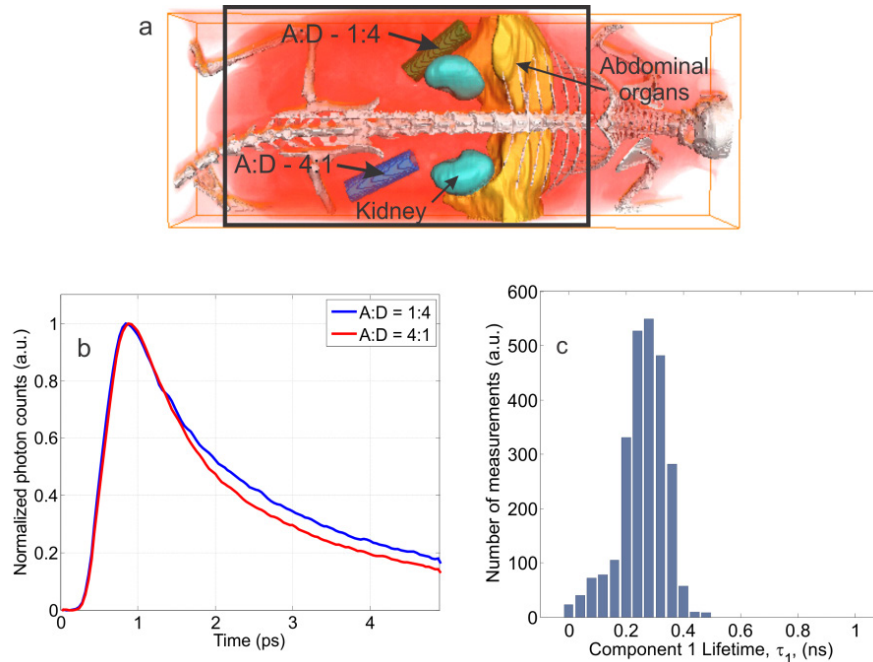
Fig. 5. a, 3D rendering of the CT images of the mouse model showing the location of two capillary tubes carrying donor acceptor mixtures with A:D ratio of 1:4 (green) and 4:1 (blue). The black border represents the registered field of view on the optical imaging platform. b, An example of the temporal measurements acquired at detectors directly above the four inclusions when excited by a full-field excitation pattern. c, Histogram of the value of shorter lifetime (FRETing donor) component for all detectors above signal threshold for all excitation patterns.

shows the histogram of estimated FRETing donor lifetime estimated using the fluorescence measurements for all 36 patterns (Mean: 0.32 ns; Std. Dev.: 0.07 ns).

The fluorescence yield was reconstructed for a 38 x 68 x 15 mm^3 volume and the 3D representation of the total reconstructed fluorescence yield is shown in Fig. 6a. It should be noted that the anatomical structures obtained from CT imaging were not included when generating weight matrices and homogeneous optical properties were assumed. This mitigated the dependence of this method on the a priori knowledge of distribution of optical properties in small animals. The 50% iso-volumes of the reconstructed fluorescence inclusions had a mean diameter of 9 mm and were accurately localized with less than 2 mm error in all three dimensions (Fig. 6b). The quantification metric derived from the relative maximum reconstructed fluorescence estimated for the FRETing donor component is shown in Fig. 6c. It should be noted that the quantitative accuracy of the method is retained when imaging optically complex volumes with less than 5% absolute error when the AD ratio is 0.25. The relatively higher f_d estimation error (~10%) observed in both studies for an AD ratio of 4 may be attributed to the limited number of time gates used in the reconstruction. The higher f_d due to the higher acceptor concentration implies a larger short lifetime component which reduces the width of the recorded temporal curve. Therefore an increased number of time gates may be required to separate the contributions from either donor species from the temporal response of the tissue.
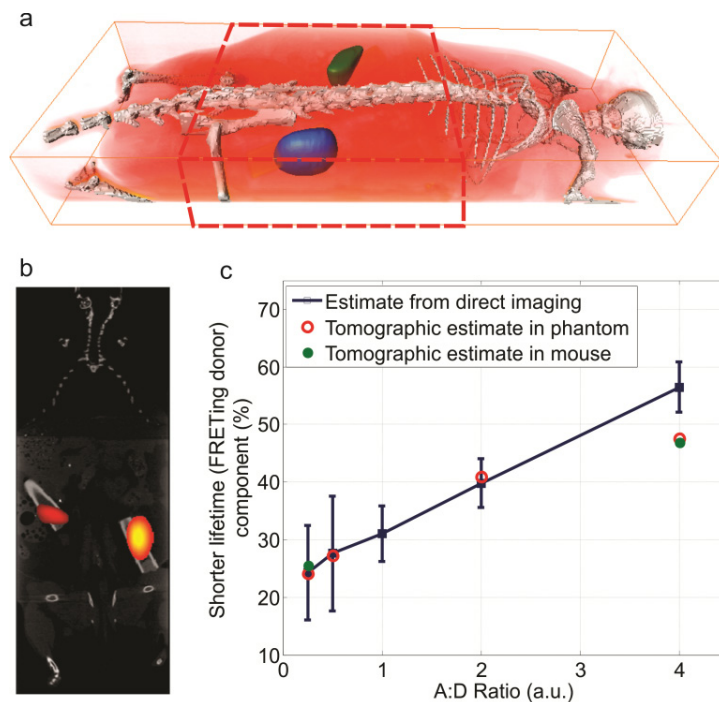
Fig. 6. a, 50% iso-volumes of total reconstructed donor quantum yield. b, The relative reconstructed quantum yield of the shorter component thresholded at 50% of maximum value overlaid on the corresponding slice from the CT volume. c, Quantitative comparison of tomographic estimates of FRETing donor fraction from above reconstruction.

5. Conclusion

Quantitative imaging of FRET activity in preclinical models promises to be a very powerful tool which will allow the study of intermolecular specific protein-protein interactions in the nanometer range in situ. The localization and quantitation of such interactions presents a challenge due to the highly diffusing transport of photons through thick tissue. The work described in this manuscript has the main goal of establishing our ability to determine the quenched donor FRET population 3D biodistribution in a quantitative manner as demonstrated by the linear relationship between acceptor/donor ratios and % quenched FRET donor both in phantom and euthanized animal. We used antibody-antigen interactions as our intermolecular FRET model as a proof of principle in solution system for receptor-ligand interaction FRET cell-based assays. The time-resolved fluorescence tomographic imaging method presented here is able to quantitatively resolve interactions between the NIR-antigen-antibody labeled probes from depths greater than 5 mm, which is well beyond the limits of current preclinical FRET imaging techniques. Through the combination of a fast wide-field time-resolved tomographic imaging platform and a computationally efficient Monte Carlo reconstruction scheme [42] based on time gate data type [26], the method described herein was able to accurately localize and quantify volumetric abundances of intermolecular FRET probes with less than 5% error. We believe this is the first presentation of such quantitative relationship, which is a crucial baseline for our ability to perform inter-molecular FRET in live animals in the future. The successful separation of FRETing and nonFRETing donor species based on lifetime contrast similar to previously reported lifetime based tomographic studies in vivo [43,44] indicates the feasibility of this approach for FRET imaging in live animal models. In particular we are currently characterizing the intermolecular FRET interactions between NIR labeled transferrin molecules upon binding to transferrin receptor at the plasma membrane. Such a NIR FRET-based assay will measure specific receptor

internalization in live animals, since transferrin molecules labeled with NIR-acceptor or donor fluorophores will only be able to FRET with each other upon binding to transferrin receptor at the plasma membrane, a step essential for the clathrin-mediated internalization of transferrin-transferrin complexes.

The ability to measure specific receptor dimerization and/or internalization in live animal imaging is a physiologically significant goal in cancer biology and drug delivery field. For instance, the stoichiometric analysis of FRET allowed by this methodology has several applications in the study of dimerization of receptors involved in cancer, e.g., epidermal growth factor receptor family (EGF-R) [45] and transferrin receptor [46], and testing of the efficacy of receptor-mediated targeted drug delivery systems in vivo [47].

Acknowledgments